

RESEARCH TECHNOLOGY

High-speed fluorescence image-enabled cell sorting

Daniel Schraivogel¹, Terra M. Kuhn^{2†}, Benedikt Rauscher^{1†}, Marta Rodríguez-Martínez^{1†}, Malte Paulsen^{3‡}, Keegan Owsley⁴, Aaron Middlebrook⁴, Christian Tischer⁵, Beáta Ramasz³, Diana Ordoñez-Rueda³, Martina Dees², Sara Cuylen-Haering^{2*}, Eric Diebold^{2*}, Lars M. Steinmetz^{1,6,7*}

Fast and selective isolation of single cells with unique spatial and morphological traits remains a technical challenge. Here, we address this by establishing high-speed image-enabled cell sorting (ICS), which records multicolor fluorescence images and sorts cells based on measurements from image data at speeds up to 15,000 events per second. We show that ICS quantifies cell morphology and localization of labeled proteins and increases the resolution of cell cycle analyses by separating mitotic stages. We combine ICS with CRISPR-pooled screens to identify regulators of the nuclear factor κ B (NF- κ B) pathway, enabling the completion of genome-wide image-based screens in about 9 hours of run time. By assessing complex cellular phenotypes, ICS substantially expands the phenotypic space accessible to cell-sorting applications and pooled genetic screening.

Fluorescence microscopy and flow cytometry are instrumental technologies used in almost all areas of biological and biomedical research. Although flow cytometric cell sorting simplifies the isolation of cells in a rapid, sensitive, and high-throughput manner, it is limited to a low-dimensional parameter space and lacks subcellular resolution (1). This method is therefore unable to capture phenotypes associated with processes involving varying signal localization, such as protein trafficking, cellular signaling, or protein mislocalization during disease (2, 3). Fluorescence microscopy, on the other hand, enables high-resolution readouts of cellular morphology and protein localization but lacks the ability to isolate cells with specific phenotypes at high speed (4). Combining the spatial resolution of fluorescence microscopy with flow cytometric cell sorting has broad implications and would inspire new experimental strategies through the rapid identification and isolation of cells with specific (sub)cellular phenotypes.

Although flow- and microfluidics-based cytometers with imaging capabilities have been developed, these approaches were unable to sort cells, came with drastically reduced throughput, or depended on nonhuman interpretable pattern recognition from raw data without image reconstruction (5–14). Furthermore, image-enabled cell sorting has so far relied on technically challenging and custom-built solutions.

To date, no system has been developed that integrates traditional flow cytometry and microscopy, operates at speeds compatible with genetic screening approaches and short-lived dynamic phenotypes, and can be operated in nonspecialized laboratories.

Here, we present a fully integrated image-enabled cell sorter (ICS) by combining (i) fluorescence imaging using radiofrequency-tagged emission (FIRE), a fast fluorescence imaging technique (15), with (ii) a traditional cuvette-based droplet sorter and (iii) new low-latency signal processing and sorting electronics (Fig. 1, A and B; for a detailed description and characterization of ICS technology, please see the materials and methods and fig. S1; for a description of the performance attributes of ICS, please see the supplementary text). To enable blur-free imaging at a high nominal flow speed of 1.1 m/s, ICS uses the FIRE approach to produce an array of 104 laser spots across 60 μ m within the core stream of the sorter cuvette, each modulated at a unique radiofrequency (Fig. 1A). The array of spots excites modulated fluorescent and scattered light from particles or cells as they flow through the optical interrogation region in the cuvette. Emitted light is collected, and the signal output is digitized and processed using low-latency, field-programmable gate arrays, allowing real-time image analysis and image-derived sort decisions. This is different from other image-enabled flow cytometers without cell-sorting capabilities (5–8, 11–13) (see the supplementary text for a comparison between technologies). To reconstruct a row of pixels from the FIRE signal for visualization of the event, the amplitude of the signal at a unique modulation frequency is assigned to a pixel value in a specific horizontal coordinate in the cuvette; in the direction of flow, the pixels are assigned a vertical location based on their temporal value, which forms a two-dimensional image of an event (Fig. 1A). The system collects scatter and fluorescent signals, as well as a

light loss signal (analogous to bright-field images produced by traditional microscopes), which allows visualization of events in real time. This contrasts with ghost cytometry, which is unable to reconstruct images from raw data in real time (10). The combination of FIRE with a cuvette-based droplet-sorter design, along with the integrated low-latency electronics, enables sorting rates at speeds of up to 15,000 events/s (fig. S1, A to C), which is comparable to traditional cell sorters and approximately one order of magnitude faster than image-activated cell sorting (9, 14). Image acquisition and high sorting rates allow immediate human interpretation of the generated data, the capture of dynamic short-lived spatial phenotypes, and the retrieval of sufficient cell numbers for downstream assays such as genome-scale screens.

To illustrate the utility of ICS for blur-free visualization of fast-flowing cells and subcellular protein distribution, we imaged a range of well-known organelles and structures of different sizes, shapes, and distributions. We were able to visualize the cell membrane, cytoplasm, membrane-enclosed organelles (nucleus, endoplasmic reticulum, Golgi apparatus, and mitochondria), and small membrane-less organelles (P bodies, Cajal bodies, and centrosomes) (Fig. 1C and fig. S2). We further demonstrated imaging of 13 cell lines of variable size and origin (fig. S3), showing the broad applicability of ICS.

For cell sorting, a set of intuitive spatial image parameters were extracted in real time from each image channel (Fig. 1B; for details of the image parameters, please see the materials and methods and fig. S4A). Image parameters were treated identically to conventional pulse parameters (area, width, and height) by the sorting electronics, allowing the combination of spatial information and traditional flow cytometry features for analysis and sorting. We demonstrate the ability of ICS parameters to quantify spatial features and to differentiate cells in a variety of applications that previously could only be distinguished using microscopy. We were able to separate cells with single or multiple/enlarged nucleoli (Fig. 2A and fig. S4C), single or multiple nuclei (Fig. 2B and fig. S4D), and distinguish cells based on cellular shape (Fig. 2C and fig. S4E). We also demonstrate the ability of ICS to reveal drug-induced organelle responses, such as the effect of brefeldin A on Golgi integrity (Fig. 2D and fig. S4F). Finally, we demonstrate the advantage of multicolor fluorescence imaging for quantification of protein localization through spatial correlation of two signals. We quantified the translocation of the nuclear factor κ B (NF- κ B) pathway component RelA from the cytoplasm to the nucleus upon tumor necrosis factor α (TNF α)-induced pathway activation, as detected by an increase in correlation between

¹Genome Biology Unit, European Molecular Biology Laboratory (EMBL), Heidelberg, Germany. ²Cell Biology and Biophysics Unit, EMBL, Heidelberg, Germany. ³Flow Cytometry Core Facility, EMBL, Heidelberg, Germany. ⁴BD Biosciences, San Jose, CA, USA. ⁵Advanced Light Microscopy Core Facility, EMBL, Heidelberg, Germany. ⁶Department of Genetics, Stanford University School of Medicine, Stanford, CA, USA. ⁷Stanford Genome Technology Center, Palo Alto, CA, USA.

*Corresponding author. Email: lars.steinmetz@embl.de (L.M.S.); eric.diebold@bd.com (E.D.); sara.cuylen-haering@embl.de (S.C.-H.)

†These authors contributed equally to this work

‡Present address: Novo Nordisk Foundation Center for Stem Cell Medicine, reNEW, Copenhagen, Denmark.

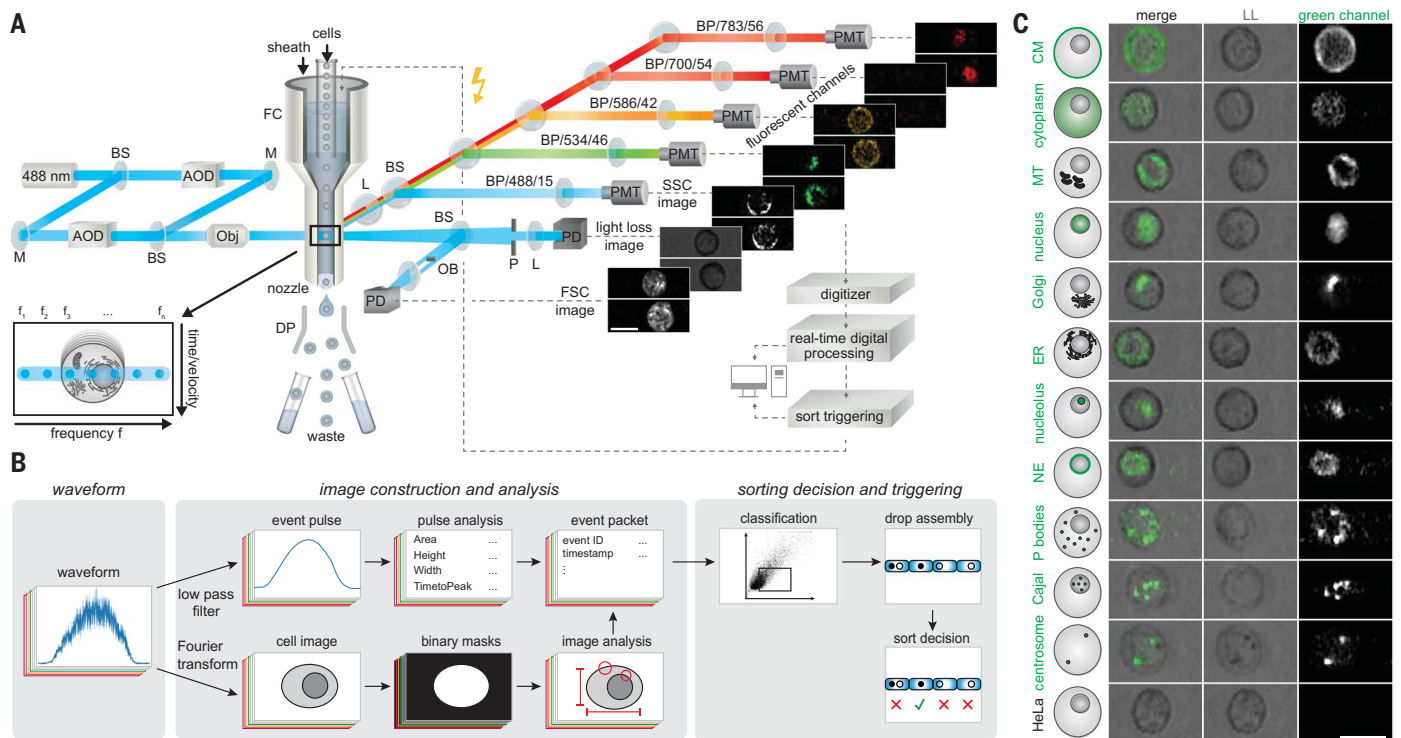


Fig. 1. Functionality of the ICS. (A) Schematic representation of the ICS optical and flow hardware components. Excitation beam path: The acousto-optic deflector (AOD) splits a single laser beam ($\lambda = 488$ nm) into an array of beamlets, each having different optical frequency and angle. A second AOD tunes the optical frequency of a reference beam, which is then overlapped with the array of beamlets. The overlapping beams intersect the flow cell (FC) of a cuvette sorter. Inset left side: The array of FIRE beams (dark cyan) are shown overlapping with the reference beam (light cyan). Because of their differing optical frequencies, the overlapping beams exhibit a beating behavior, which causes each beamlet to carry a sinusoidal modulation at a distinct frequency f_{1-n} . Emission beam path: Images are generated from digitized signals on a per-event basis and include light loss, forward scatter (FSC), and side scatter (SSC) images, and four different fluorescent channels. Example images: HeLa cells expressing the Golgi marker GalNAct2-green fluorescent protein (GFP) (green) were stained with cell surface marker CD147 PE-CF594 (orange) and DRAQ5 nuclear dye (red). FSC, SSC, and light loss images are shown in grayscale. BS, beam splitter; M, mirror; Obj, objective; DP, deflection plates; OB, obscuration bar; P, pinhole; L, lens; BP, band pass; PMT, photomultiplier tube; PD, photodiode. Scale bar, 20 μm . (B) Overview of the ICS low-latency data-processing pipeline. Each

photodetector produces a pulse with high-frequency modulations encoding the image (waveform). Fourier analysis is performed to reconstruct the image from the modulated pulse. An image-processing pipeline produces a set of image features (image analysis), which are combined with features derived from a pulse-processing pipeline (event packet). Real-time sort classification electronics then classify the particle on the basis of image features, producing a sort decision that is used to selectively charge the droplets (dotted gray line in A). (C) ICS-based imaging of HeLa cells expressing GFP- or mNG-tagged fluorescent proteins or stained with organelle-specific green fluorescent dyes. One representative image is shown per organelle; the full datasets containing 10,000 images each are shared as described in the data and materials availability section. The following dyes or protein fusions were used: cell membrane (Cellmask dye), cytoplasm (GFP fused to HIV Rev nuclear export sequence), mitochondria (Mitotracker dye), nucleus (H2B-mNG), Golgi apparatus (GalNAct2-GFP), endoplasmic reticulum (ER, ERTracker dye), nucleolus (eGFP-Ki-67), nuclear envelope (LamB1-GFP), P bodies (eGFP-DDX6), Cajal bodies (eGFP-COIL), and centrosomes (anti-pericentrin antibody). P bodies and Cajal bodies were recorded from fixed cells, centrosomes from fixed and metaphase-stalled cells; fixation resulted in decreased contrast in the light loss (LL) image. Scale bar, 20 μm .

RelA and the nuclear dye DRAQ5 (Fig. 2E and fig. S4G). These experiments illustrate the utility of ICS parameters for quantification, and ultimately sorting, of a broad spectrum of phenotypes.

To demonstrate the cell-sorting functionality of the ICS, we applied it to the mitotic cell cycle, a dynamic process associated with multiple complex phenotypic changes. Traditional flow cytometry can separate three cell cycle stages, G_1 , G_2 /mitosis, and S phase, but fails to distinguish cells in different mitotic stages. Although chemicals that block mitosis can be used to enrich certain stages (notably excluding anaphase and telophase) (16–18), these approaches can alter gene expression and post-

translational modifications. We demonstrate that ICS can isolate the mitotic stages of HeLa cells by using H2B-mNeonGreen (mNG) to visualize chromatin and the intensity of phosphorylated serine 10 on histone H3 (pS10H3) as a marker associated with mitotic chromatin condensation (19). We investigated cells from the G_2 /mitosis phases of the univariate cell cycle and created a training dataset by manually classifying 100 cells from each stage throughout mitosis (Fig. 2F; for a description of the criteria used to distinguish mitotic stages, please see the materials and methods). Classified events were organized on a trajectory in chronological order (fig. S5A). We used this training dataset to identify the most differ-

ing image-, scatter- and intensity-based parameters between stages by fitting a decision tree model and performing feature importance analysis (20) (Fig. 2G and fig. S5B). Image-derived parameters dominated the most differentiating parameters, such as maximum intensity, radial moment, and eccentricity of the H2B-mNG signal that differentiated among metaphase, anaphase, and telophase cells (Fig. 2H). We used these features to establish a hierarchical gating strategy for cell sorting and performed independent microscopic validation of the isolated populations (Fig. 2I). We found that ICS isolated highly pure populations, including G_2 interphase (96% purity), prometaphase (64%), metaphase (78%), anaphase (94%),

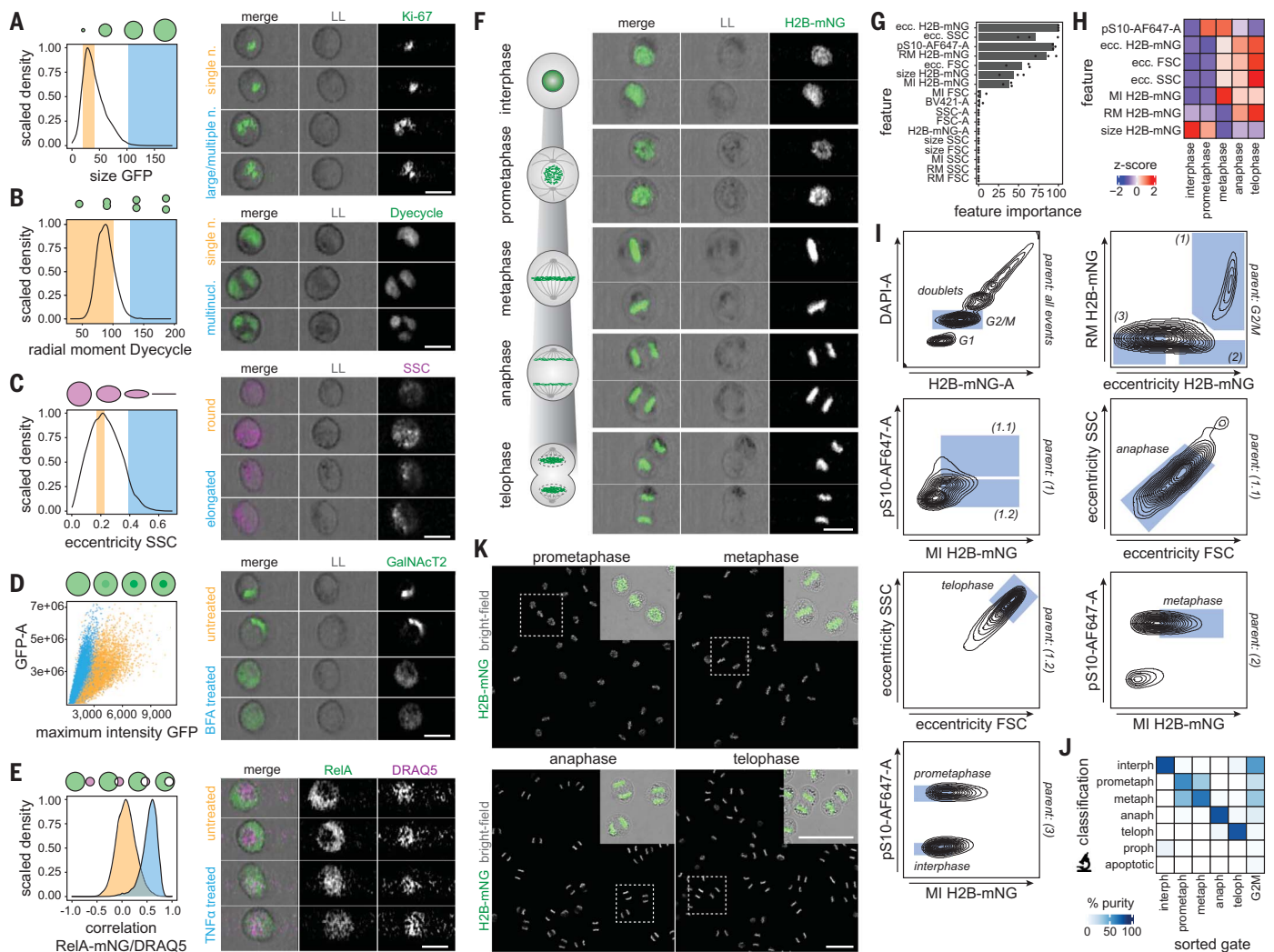


Fig. 2. ICS measurements quantify spatial cellular processes and isolate phenotypes of interest.

(A) HeLa cells expressing eGFP-Ki-67 were gated for singlets and live cells, and the ICS size parameter of the eGFP-Ki-67 signal was used to distinguish between cells with single small nucleoli and those with multiple or large nucleoli. Size is defined by the number of pixels above a user-defined threshold. n, nucleolus. Scale bar, 20 μm .

(B) HeLa cells stained with the nuclear dye DyeCycle Green were gated for singlets and live cells, and the radial moment of DyeCycle Green was used to differentiate cells with single or multiple nuclei. Radial moment is the mean-square distance of the signal from the centroid. n, nucleus. Scale bar, 20 μm .

(C) HeLa cells were gated for singlets and live cells, and the eccentricity calculated from the side scatter image was used to distinguish round from elongated cells. Eccentricity was computed by first finding the magnitudes of the spread along the two principal components of the image, then taking their ratio. Scale bar, 20 μm .

(D) HeLa cells expressing the Golgi marker GalNACT2-GFP were gated for singlets and live cells and either treated with brefeldin A (BFA) or left untreated. The maximum intensity of the GalNACT2-GFP channel was used to distinguish treated from untreated cells, whereas the overall GFP intensity (y axis) was largely unaffected by the treatment. Maximum intensity is the value of the brightest pixel. A, area. Scale bar, 20 μm .

(E) HeLa cells expressing RelA-mNG were treated with TNF α or left untreated and stained with the cell-permeable nuclear dye DRAQ5. Cells were then gated for singlets and live cells, and the correlation between RelA-mNG and DRAQ5 was used to differentiate between the treated (nuclear RelA) and untreated (cytoplasmic RelA) conditions. Correlation is the Pearson's correlation score between the intensities of the pixel values from

two imaging channels. Scale bar, 20 μm .

(F) HeLa cells expressing H2B-mNG were synchronized to increase the frequency of rare mitotic stages and released into mitosis without chemical perturbation. Then, cells were fixed for labeling with an antibody recognizing phosphorylated serine 10 on histone H3 (pS10H3) to allow microscopic validation after sorting. Samples were stained with 4',6-diamidino-2-phenylindole (DAPI) for univariate cell cycle analysis. Representative images of individual cells within the G₂/M population reveal captures of major mitotic stages. LL, light loss. Scale bar, 20 μm .

(G) A decision tree model was trained to distinguish the mitotic stages of manually classified datasets ($n = 100$ per stage, three replicate recordings and classifications). Shown are the results of a feature importance analysis of ICS measurements representing the summarized reduction in the loss function attributed to each feature at each split in the tree. RM, radial moment; ecc, eccentricity; MI, maximum intensity.

(H) Feature values from (G) were standardized, and median values for cells and from three replicates of classified datasets are shown as a heatmap. Only features that vary between the mitotic stages are shown [variable importance >0 in (G)].

(I) On the basis of the identified features in (H), a hierarchical gating strategy was built that enriches for interphase, prometaphase, metaphase, anaphase, and telophase stages.

(J) A total of 5000 cells were sorted for microscopic validation based on the gating strategy established in (I), and manual classification from confocal z stacks of the sorted cells was performed. Shown are mean percentages of three independent replicates. Prometaphase cells were generated by two consecutive sorts (see the materials and methods). interph., interphase.

(K) Representative single-slice confocal fluorescence microscopy images from sorted cells from (J) with bright-field/H2B-mNG overlays as inlays. Scale bar, 50 μm .

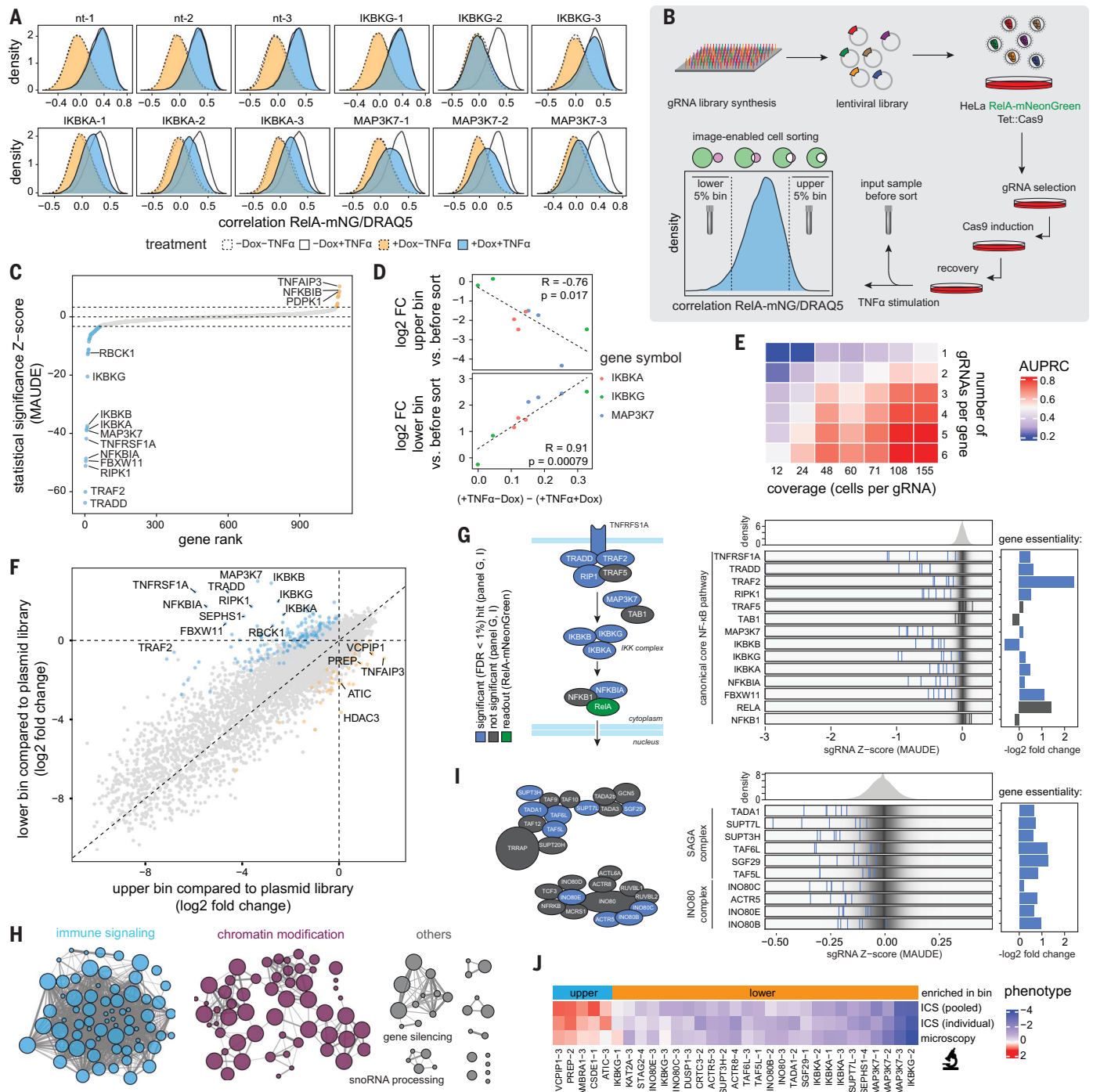


Fig. 3. ICS detects the effects of CRISPR perturbations and enables pooled genetic screens of protein localization. (A) Effects of individual CRISPR perturbations on RelA nuclear translocation. HeLa cells with Tet-inducible Cas9 and stably expressing RelA-mNG were transduced with gRNA-1, gRNA-2, and gRNA-3 targeting the core NF- κ B pathway proteins IKBKG, IKBKA, and MAP3K6, respectively, or with nontargeting (nt) control gRNAs. gRNA expression was induced with doxycycline (Dox) or left uninduced. Correlation between RelA-mNG and DRAQ5 was quantified using ICS as a measurement for RelA nuclear translocation in the presence or absence of TNF α . (B) Overview of the pooled CRISPR screening setup and readout using ICS. Positive regulators of RelA nuclear translocation are enriched in the lower bin and depleted from the upper bin. Tet::Cas9, tetracycline/doxycycline-inducible Cas9. (C to E) Results

of the ICS-based CRISPR screen using an NF- κ B pathway-focused library ($n = 1068$ genes). (C) The screen was performed at different library coverages, and reads from collected samples were combined in silico to a high-coverage (359 cells per gRNA per sorted bin) dataset. Hits were called using the software MAUDE (26). Genes are ranked by their statistical significance and selected positive/negative regulators are highlighted. The horizontal dashed lines indicate an FDR of 1%, whereas genes with FDR <1% are marked in cyan and orange, respectively. (D) Comparison of phenotypes measured in individual perturbation experiments from (A) (x axis) or the pooled screen (y axis) using the same gRNAs. For the pooled screen, differences in gRNA abundance in the upper (top panel) and lower (bottom panel) sorted bins compared with the input sample were determined from the high-coverage dataset in (C). R values represent

Pearson correlation coefficients. FC, fold change. (E) Screen hits as determined at different library coverages (12 to 155 cells per gRNA per sorted bin) using between one and six gRNAs per gene were compared with a high-coverage reference sample (359×, six gRNAs per gene) by precision-recall analysis. Heatmap shows AUPRC values for different levels of library coverage and different numbers of gRNAs per gene. (F to J) Results of the ICS-based genome-wide screen ($n = 18,408$ genes). (F) Scatter plot of fold changes visualizing gRNA abundance changes in upper (x axis) and lower (y axis) sorted bins compared with the plasmid library. Cyan and orange dots indicate statistically significant positive and negative regulators, respectively (FDR <1% according to MAUDE). (G) Genome-wide CRISPR screen identified core canonical NF- κ B pathway components. Left panel: Schematic of the core canonical NF- κ B signaling pathway. Right top panel: Distribution of the gRNA Z-score for the whole genome-wide library. Right panels: gRNA Z-score for individual gRNAs per gene overlaid with a gradient (grayscale) depicting overall Z-score distribution. Right bar chart: Gene essentiality as determined by the \log_2 FC of the gRNA abundance in the unsorted cell population

compared with the plasmid library. (H) GO network of hits with FDR <1%, colored by modules identified from protein–protein interactions using STRING-db (45). Gray lines connect associated GO terms, edges represent GO terms. Names of individual edges were omitted, clusters that were not associated with immune signaling or chromatin modification were collected in a third class called “others.” (I) Screen results for SAGA and INO80 protein complex components. Left panel: Schematic illustration of the SAGA and INO80 protein complexes. Right panels: As described in (G). (J) Selected hits from the genome-wide screen (one gRNA per gene; we picked the gRNA that showed the strongest Z-score in the pooled genetic screen) were validated using two orthologous methods (individual validation using ICS, and individual validation using microscopy). The top row in the heatmap shows the phenotypes measured in the genome-wide screen (MAUDE Z-score). The phenotype in the second and third rows of the heatmap represents the standardized difference in signal medians between the knockout and control gRNA cell populations. Nuclear RelA abundance was quantified using microscopy by measuring the correlation between RelA-mNG and DRAQ5.

and telophase (93%) (Fig. 2, J and K, and fig. S5, C to E). With these advances, we increased the resolution of flow cytometric cell cycle analyses to the level of distinguishing individual mitotic stages (including the thus-far inaccessible anaphase and telophase stages), yielding a method for robust enrichment of high numbers of cells in the absence of chemical blockers and from the same source sample. Isolated cells can be used in numerous downstream applications, such as the comparison of stage-specific changes in transcriptome, chromatin architecture, or protein modifications.

Pooled functional genomic screens with microscopic readouts have so far been limited in throughput and depended on technically challenging methods (21–25). ICS allows high-speed cell isolation based on fluorescence spatial information, and therefore has the potential to increase the scale and speed of microscopy-based screens and reduce technical complexity, duration, and cost. We tested the compatibility of ICS with pooled CRISPR screens by examining the nuclear translocation of RelA upon NF- κ B pathway activation, a process that is invisible to traditional flow cytometry. To measure RelA translocation upon CRISPR-mediated perturbation, we quantified RelA-mNG/DRAQ5 spatial correlation (Fig. 2E) in HeLa cells expressing Tet-inducible Cas9 and fluorescently tagged RelA (23) (HeLa RelA) (fig. S6, A to C). We validated the approach using individual CRISPR knockouts of three core NF- κ B pathway components, IKKBA, IKKKG, and MAP3K7, and found consistent defects in RelA nuclear translocation upon gene knockout, demonstrating that ICS sensitively captures the effects of these perturbations (Fig. 3A and fig. S6D). Next, we proceeded with a pooled screen in which a population of Cas9-expressing cells is transduced with a mixture of guide RNAs (gRNAs). We transduced HeLa RelA cells with an NF- κ B pathway–focused library targeting 1068 genes, including 37 NF- κ B core canonical pathway components. Cells were then treated with TNF α , and the 5% lower (cytoplasmic

RelA) and upper (nuclear RelA) bins of the RelA-mNG/DRAQ5 correlation parameter were isolated (Fig. 3B and fig. S7A). Sorting was conducted with an average event rate of 4000 events/s, a speed comparable to current flow-based technology for large cells such as HeLa, enabling a 100× coverage of a 1000 gRNA library in <9 min. Bulk sorts were performed at different library coverage to determine optimal library coverage and gRNA number per gene. We generated a “ground-truth” high-coverage (359-fold) dataset by pooling all reads from the differently sized samples, followed by gRNA hit calling (26). Among the most significant hits, we identified known NF- κ B pathway components, demonstrating that ICS can identify bona fide regulators of the NF- κ B pathway (Fig. 3C and table S1). We found strong correlation between the individual and pooled perturbations, indicating that both perturbation strategies rank genes similarly (Fig. 3D and fig. S7B). Next, we investigated how the number of gRNAs per gene and library coverage affect hit-calling performance. High performance [area under the precision recall curve (AUPRC) >0.7; 70% of hits detected at <1% false discovery rate (FDR)] was achieved with only 100 cells per gRNA and three gRNAs per gene (Fig. 3E and fig. S7, C and D). Performance increased with library coverage and number of gRNAs per gene, because sporadic false hits caused by gRNA dropouts in the low-coverage samples decreased (fig. S7, E and F). Independent screen replicates showed high reproducibility ($0.77 \leq R \leq 0.87$; fig. S7G).

To fully exploit the high-speed capabilities of ICS, we next sought to identify NF- κ B pathway regulators globally in a genome-wide screen. We generated a new genome-wide CRISPR/Cas9 library targeting 18,408 protein-coding genes with fully adjustable numbers of gRNAs per gene (fig. S8 and supplementary text). Using six gRNAs per gene and a 100× library coverage, we identified 169 hits (FDR <1%), encompassing 133 positive and 36 nega-

tive regulators (Fig. 3F, fig. S9A, table S2, and supplementary text). A down-sampling–based analysis confirmed that three gRNAs per gene ranked genes similarly to the full library of six gRNAs (fig. S9, B and C). Among these hits, we identified all core canonical NF- κ B pathway components except for three pathway genes, TRAF5, TAB1, and NFKB1, consistent with previous reports of these genes not being essential for pathway functionality (23, 27–29) (Fig. 3G). To identify potential new regulators, we performed a Gene Ontology (GO) term-based network analysis, which showed marked enrichment of a cluster of processes centered around chromatin modification (Fig. 3H). Among the underlying genes, we identified the histone deacetylase HDAC3, which induces RelA nuclear export during pathway shutdown (30). We also found previously unknown regulators including multiple components of the SAGA chromatin-acetylation complex (31) and the INO80 chromatin-remodeling complex (32), indicating a previously unknown role of these complexes in NF- κ B pathway regulation (Fig. 3I and supplementary text). For hit validation, we assessed the top 10 previously unknown positive and negative candidates, the 10 identified members of the SAGA and INO80 complexes, and three known NF- κ B pathway components. Individual CRISPR knockouts followed by quantification of RelA nuclear translocation using both ICS and microscopy revealed strong agreement ($0.857 \leq R \leq 0.908$) between these measurements and confirmed the observations from the pooled genetic screen (Fig. 3J and fig. S9, D and E). In addition, our validation experiments indicate that ICS can reach similar accuracy and ranks genes similarly to fluorescence microscopy (Fig. 3J and fig. S9D). With the applied event rate of 4000 events/s, ICS is significantly faster compared with recently developed microscopy-based methods for pooled genetic screens (22–25) (for comparison, see the supplementary text) and enabled the completion of a genome-wide screen (three gRNAs per

gene, 100× coverage) within only 9 hours of run time.

In conclusion, ICS substantially expands the phenotypic space accessible to cell-sorting applications and functional genomic screening. This method meets the requirements of high-speed cell sorting, multicolor fluorescence imaging, and full integration into a device that can be operated in nonspecialized laboratories. This will ensure broad availability and inspire new experimental strategies in diverse areas, including basic research, cell-based diagnostics, cell atlas efforts (3), and high-content image-based screening (2, 33, 34). With the potential to include downstream (multi)omics readouts (35–41), ICS provides a fundamentally new capability for probing deep into the molecular mechanisms underlying cell physiology and protein localization.

REFERENCES AND NOTES

1. A. Cossarizza et al., *Eur. J. Immunol.* **49**, 1457–1973 (2019).
2. M. Boutros, F. Heigwer, C. Laufer, *Cell* **163**, 1314–1325 (2015).
3. P. J. Thul et al., *Science* **356**, eaal3321 (2017).
4. V. Espina et al., *Nat. Protoc.* **1**, 586–603 (2006).
5. A. S. Rane, J. Rutkauskaite, A. DeMello, S. Stavrakis, *Chem* **3**, 588–602 (2017).
6. K. Goda et al., *Proc. Natl. Acad. Sci. U.S.A.* **109**, 11630–11635 (2012).
7. H. E. Muñoz et al., *Anal. Chem.* **90**, 11280–11289 (2018).
8. T. Miura et al., *Biomed. Opt. Express* **9**, 3424–3433 (2018).
9. N. Nitta et al., *Cell* **175**, 266–276.e13 (2018).
10. S. Ota et al., *Science* **360**, 1246–1251 (2018).
11. G. Holzner et al., *Cell Rep.* **34**, 108824 (2021).
12. T. C. George et al., *Cytometry A* **59**, 237–245 (2004).
13. H. Mikami et al., *Nat. Commun.* **11**, 1162 (2020).
14. A. Isozaki et al., *Lab Chip* **20**, 2263–2273 (2020).
15. E. D. Diebold, B. W. Buckley, D. R. Gossett, B. Jalali, *Nat. Photonics* **7**, 806–810 (2013).
16. P. Clute, J. Pines, *Nat. Cell Biol.* **1**, 82–87 (1999).
17. G. W. Zieve, D. Turnbull, J. M. Mullins, J. R. McIntosh, *Exp. Cell Res.* **126**, 397–405 (1980).
18. J. Jackman, P. M. O'Connor, *Curr. Protoc. Cell Biol.* **Chapter 8**, Unit 8.3 (2001).
19. C. Prigent, S. Dimitrov, *J. Cell Sci.* **116**, 3677–3685 (2003).
20. P. Wei, Z. Lu, J. Song, *Reliab. Eng. Syst. Saf.* **142**, 399–432 (2015).
21. E. C. Wheeler et al., *Nat. Methods* **17**, 636–642 (2020).
22. C. Wang, T. Lu, G. Emanuel, H. P. Babcock, X. Zhuang, *Proc. Natl. Acad. Sci. U.S.A.* **116**, 10842–10851 (2019).
23. D. Feldman et al., *Cell* **179**, 787–799.e17 (2019).
24. G. Kanfer et al., *J. Cell Biol.* **220**, e202006180 (2021).
25. X. Yan et al., *J. Cell Biol.* **220**, e202008158 (2021).
26. C. G. de Boer, J. P. Ray, N. Hacohen, A. Regev, *Genome Biol.* **21**, 134 (2020).
27. K. Tada et al., *J. Biol. Chem.* **276**, 36530–36534 (2001).
28. C. Wang et al., *Nature* **412**, 346–351 (2001).
29. L.-F. Chen, W. C. Greene, *Nat. Rev. Mol. Cell Biol.* **5**, 392–401 (2004).
30. L.-F. Chen, W. Fischle, E. Verdin, W. C. Greene, *Science* **293**, 1653–1657 (2001).
31. D. Helmlinger, L. Tora, *Trends Biochem. Sci.* **42**, 850–861 (2017).
32. L. Chen et al., *J. Biol. Chem.* **286**, 11283–11289 (2011).
33. Y. Feng, T. J. Mitchison, A. Bender, D. W. Young, J. A. Tallarico, *Nat. Rev. Drug Discov.* **8**, 567–578 (2009).
34. Z. E. Perlman et al., *Science* **306**, 1194–1198 (2004).
35. D. Schraivogel et al., *Nat. Methods* **17**, 629–635 (2020).
36. D. A. Jaitin et al., *Cell* **167**, 1883–1896.e15 (2016).
37. P. Datlinger et al., *Nat. Methods* **14**, 297–301 (2017).
38. A. Dixit et al., *Cell* **167**, 1853–1866.e17 (2016).
39. G. X. Y. Zheng et al., *Nat. Commun.* **8**, 14049 (2017).
40. P. Shahi, S. C. Kim, J. R. Haliburton, Z. J. Gartner, A. R. Abate, *Sci. Rep.* **7**, 44447 (2017).
41. M. Stoeckius et al., *Nat. Methods* **14**, 865–868 (2017).
42. B. Rauscher, C. Tischer, K. Owsley, D. Schraivogel, L. Steinmetz, *Zenodo* (2021).
43. U. Sarkans et al., *Nucleic Acids Res.* **46**, D1266–D1270 (2018).
44. J. Spidlen, K. Breuer, C. Rosenberg, N. Kotecha, R. R. Brinkman, *Cytometry A* **81**, 727–731 (2012).
45. D. Szklarczyk et al., *Nucleic Acids Res.* **47**, D607–D613 (2019).

ACKNOWLEDGMENTS

We thank L. Velten, J.-K. Heriche, R. Kumar, A. Kreshuk, and T. Alexandrov for input on computational analyses; R. Pepperkok, S. Reither, A. Hauth, F. Stuedle, D. Gerlich, J. Zuber, M. Knop, Y. Hayashi, E. Schiebel, J. Ellenberg, and J. Kornienko for providing cell lines, antibodies, and constructs; M. Rogon for network analysis support; M. Krause, D. Schichler, A. Hughes, and P. Jakob for experimental support; BD Biosciences, a unit of Becton, Dickinson and Company; the BD CellView team that developed the BD CellView Imaging Technology that enabled ICS (contributing team members are listed in the supplementary text); J. Horta and D. Fantin for managerial support; J. Kim and D. Martin for instrument support and maintenance; the EMBL Advanced Light Microscopy Facility (ALMF) for support; the EMBL Genecore for next-generation sequencing services; V. Benes for advice; the EMBL Flow Cytometry Core facility for flow cytometry support, advice, and instrument maintenance; and L. Velten, K. Zeier, J. Horta, and M. Bao (Life Science Editors) for input on the manuscript. **Funding:** This work was supported by grants from the European Research Council (Advanced Investigator Grants AdG-294542 and AdG-742804 to L.M.S.), the German Research Foundation (DFG project number 402723784 to S.C.-H.), and the

Human Frontier Science Program (CDA00045/2019 to S.C.-H.). D.S. was supported by a fellowship from the EMBL Interdisciplinary Postdoc (EIPOD) program (Marie Skłodowska-Curie Actions COFUND grant agreement 664726). T.M.K. was supported by a postdoctoral fellowship from the European Molecular Biology Organization (EMBO ALTF 1154-2020). C.T. was supported by the Chan Zuckerberg Initiative DAF, an advised fund of the Silicon Valley Community Foundation (grant 2020-225265). M.P. was supported by the Novo Nordisk Foundation (grants NNF17CC0027852 and NNF21CC0073729). **Author contributions:** D.S., M.P., A.M., S.C.-H., and L.M.S. conceptualized the project. D.S., T.M.K., M.R.-M., M.P., and M.D. performed experiments. T.M.K. and S.C.-H. collected and analyzed microscopy data. B.Rau. designed CRISPR libraries. D.S. and M.R.-M. performed functional genomics screens. B.Ram. and D.O. supported flow cytometric experiments. B.Ram. performed purity sorts. D.O. performed instrument QC. B.Rau., K.O., and D.S. performed bioinformatic analysis. C.T. wrote Fiji plugins. K.O., A.M., and E.D. developed BD CellView Imaging Technology. D.S., B.Rau., M.R.-M., T.M.K., M.P., K.O., A.M., S.C.-H., E.D., and L.M.S. wrote the manuscript. All authors read and commented on the manuscript. **Competing interests:** K.O. and/or E.D. are inventors on patents 9423353, 9983132, 10078045, 10324019, 10006852, 10408758, 10823658, 10578469, 10288546, 10684211, 11002658, 10620111, 11105728, 10976236, 10935482, and 11055897 held or licensed for use by Becton, Dickinson and Co. that cover BD CellView Imaging Technology. K.O., A.M., and E.D. are employees at BD Biosciences. BD CellView, BD FACS Melody, BD FACS Aria, BD FACSCorpus (and any others used) are trademarks or registered trademarks of Becton, Dickinson and Company. **Data and materials availability:** NGS data from gRNA library and targeted genome sequencing were deposited at the Gene Expression Omnibus (GSE167944). Documented code to reproduce all analyses and figures was deposited at GitHub (<https://github.com/benediktrauscher/>) and Zenodo (42). Fiji tools and source code thereof were deposited at GitHub (<https://github.com/embl-cba/ICS>) and Zenodo (42). ICS image data were deposited on the BioImage Archive (43) (S-BSST644, available from <https://www.ebi.ac.uk/biostudies/>). Flow cytometry data were deposited at <https://flowrepository.org> (44) (FR-FCM-Z4M5). Metadata and archiving information for ICS data are provided in table S3. Plasmid “phage UbiC tagRFP-T-DDX6” is available under a material transfer agreement from Addgene. Cell line “HeLa Tet:Cas9 RelA-mNeonGreen” is available under a material transfer agreement from Broad Institute (P. Blainey).

SUPPLEMENTARY MATERIALS

[science.org/doi/10.1126/science.abj3013](https://doi.org/10.1126/science.abj3013)
Materials and Methods
Supplementary Text
Figs. S1 to S10
Tables S1 to S7
References (46–102)
MDAR Reproducibility Checklist

[View/request a protocol for this paper from Bio-protocol.](#)

27 May 2021; accepted 8 December 2021
10.1126/science.abj3013

High-speed fluorescence image-enabled cell sorting

Daniel SchraivogelTerra M. KuhnBenedikt RauscherMarta Rodríguez-MartínezMalte PaulsenKeegan OwsleyAaron MiddlebrookChristian TischerBeáta RamaszDiana Ordoñez-RuedaMartina DeesSara Cuylen-HaeringEric DieboldLars M. Steinmetz

Science, 375 (6578), • DOI: 10.1126/science.abj3013

Sorting cells by intracellular features

Fluorescence-activated cell sorting, reported in *Science* 52 years ago, has revolutionized biomedical research, giving us the ability to isolate cells according to the expression of labeled proteins. So far, however, flow cytometric cell sorting has been blind to spatial processes such as intracellular protein localization, which is traditionally measured using microscopy. Schraivogel *et al.* combined ultrafast microscopy and image analysis with a flow cytometric cell sorter to unlock spatial phenotypes for high-throughput sorting applications. The authors show how this technology can be used to rapidly isolate cells with complex cellular phenotypes and how it can accelerate genome-wide microscopy-based CRISPR screening. —DJ

View the article online

<https://www.science.org/doi/10.1126/science.abj3013>

Permissions

<https://www.science.org/help/reprints-and-permissions>

Use of think article is subject to the [Terms of service](#)

Science (ISSN) is published by the American Association for the Advancement of Science. 1200 New York Avenue NW, Washington, DC 20005. The title *Science* is a registered trademark of AAAS.

Copyright © 2022 The Authors, some rights reserved; exclusive licensee American Association for the Advancement of Science. No claim to original U.S. Government Works